Energy Optimal Attitude Control and Task Execution for a Solar-Powered Spacecraft*

Bjørn Andreas Kristiansen[1], Jan Tommy Gravdahl[1], Sebastien Gros[1], Tor Arne Johansen[1]

Abstract—In this article, we aim to maximize the net energy a solar-powered spacecraft gains when performing a sequence of tasks leading to attitude maneuvers over the spacecraft's orbit, including an eclipse. The net energy can be defined as the integral of the power supplied by the solar panels minus the power used by the payload and satellite systems, including the attitude control system. The energy flow depends on both the power spent on the satellite electronic systems and the power received from the solar panels. Thus, the optimal attitude control problem is formulated so that the attitude of the spacecraft relative to the Sun during the maneuver is included in the calculations in addition to the actuation cost. This paper proposes a cost function based on net energy to address this problem, introducing a cost function that incorporates the incoming energy from the solar irradiance and the outgoing energy due to actuation. A function that differentiates between the eclipse's fully and partially shaded regions is added to simulate the solar irradiance in an eclipse. Our approach is demonstrated in a simulation study where the HYPSO-2 Earth observation satellite executes a sequence of imaging, communication, and energy-harvesting tasks. HYPSO-2 is a 6U CubeSat equipped with deployable solar cell arrays, and the optimal control problem is solved using IPOPT in CasADi.

Index Terms—attitude control, energy optimal control, optimization, aerospace control

I. INTRODUCTION

Attitude control for spacecraft is a well-known problem [1]. Regarding optimal attitude control, research has been conducted with various cost functions. Optimization with respect to time is common; see for example [2]–[5]. Others have proposed optimal attitude control schemes with generalized cost functions [6], [7]. Optimization with respect to cost functions based on angular velocities has been studied in [8]. The authors in [9] and [10] used power models for optimization. In [9], the authors exploited a power model based on the energy lost due to the system's mechanics, while [10] use a power model based on the power available in a control moment gyroscope. Minimizing with respect to energy functions based on the input, for example by using a performance index [11] or an input-related norm [12], is a popular approach. Another name for the minimization of the input is minimal effort [5]. Minimizing the norm of the input has often been considered energy optimal. The authors in [13] define the optimal control problem of minimizing the square

of the input as the optimal energy approach. The contribution of this paper is to show that solar power harvesting should be included in the optimization alongside the power consumption term to achieve energy-optimal control. This influences how the cost function here is designed: in this paper, we propose a physics-based cost function based on net electric power that we then use to achieve the minimal-energy cost control objective.

The optimal control problem in [14] has similarities to the work in [15] and this paper. The authors of [14] optimize with respect to what here is referred to as the solar power of the spacecraft only and not the entire net power cost introduced in [15], which this paper is based on. In addition to this difference, we make efforts to formulate our optimal control problem in a way that makes it possible to solve the problem as a nonlinear program (NLP) through direct multiple shooting, whereas [14] solves their problem as a mixed-integer program.

In [15], the net power cost function is introduced and tested through simulations over a short period of time using three orthogonal reaction wheels. The simulations were performed entirely in the sun, and thus the eclipse was not considered. In the present paper, we expand on the formulation of the optimal control problem in [15]: In addition to the introduction of some known disturbances, or perturbations, we refine the definition of the net power cost function by including a definition of a function labeled $\delta(\cdot, \cdot)$, which returns the amount of solar irradiance the spacecraft experiences based on its position relative to a potentially occluding body (the Earth). The function is defined here so that it describes both the penumbra and umbra regions of the eclipse, thus introducing a physics-based transition between the periods where the spacecraft is exposed to sunlight and when it is in eclipse. Note that [14] also introduces a function where the Earth shadow is defined, but this shadow is defined as a constant value for the entire eclipse, and does therefore not include different values for the penumbra and the umbra regions, as we have done in this paper. The argument for including the penumbra is, among others, made in [16], where the author emphasizes the region's significance in determining the amount of power available to the spacecraft.

In this paper, we perform simulations based on a scenario where the spacecraft moves in and out of eclipse during the scenario, an extension of [15]. The spacecraft for the studied mission, which has four reaction wheels, has an extra set of actuators in the form of magnetorquers, which are also included in the actuation cost. The magnetorquers are primarily meant to manage momentum, but their power consumption is included in the optimal control problem. Using

this expanded model, we explore the use of the net power cost function introduced in [15] for a scenario from the upcoming HYPSO-2 mission.

HYPSO-2 is an Earth observation mission that uses a push-broom hyper-spectral imager to achieve its objectives, primarily for observing ocean color, water quality, and algal blooms. HYPSO-2 is similar to the HYPSO-1 mission, see [17], but will, due to increased downlink capacity, be more constrained primarily by its solar energy harvesting capacity rather than the amount of data the satellite could downlink as is the case with HYPSO-1. To improve the resolution of the images, the spacecraft, a 6U CubeSat can perform a slewing maneuver at a constant angular rate over the target area. Besides the time spent on image acquisition (slew maneuver), the satellite will spend most of its time harvesting solar energy. While the slewing maneuver can be interesting from a control perspective [18], [19], this paper focuses on what happens between the slewing (imaging) and communication pointing maneuvers, where the primary objective of the attitude control system is to gather as much energy as possible while executing data processing and communication tasks. HYPSO-2 will be equipped with deployable solar panels, another aspect that is also considered when formulating the optimal control problem.

The contributions of this paper are the following: we extend the net electric energy cost function introduced in [15] to account for a deployable solar panel. We include a mathematical formulation for the amount of solar irradiance the satellite's solar panels receive and extend the cost function to allow for magnetorquers. The cost function and model are refined to allow more than three reaction wheels. Based on the extended attitude control scenario where a sequence of maneuvers results from a typical sequence of imaging and communication tasks, we argue for the increased benefit of using the proposed method for satellites as the frequency of attitude maneuvers increases.

The remaining sections of this paper are organized as follows: The novel cost function, defined as the sum of the incoming solar power and the actuation power consumption of the system in [15], is defined and expanded upon in Section II. The optimal control problem itself is stated in Section III, both in a general form and using the frames introduced in Section Section II, using unit quaternions to represent the spacecraft's attitude. Section V defines the PD controller used for the initial guesses to the optimal solver and as a baseline. It also contains the optimal control problem that defines the references for the sun-pointing PD controller as previously introduced in [15]. Section VII describes the setup for the numerical example using the net energy cost function based on the HYPSO-2 mission. The results in Section VIII show how the optimal net energy solution performs for the given control scenario. The results are discussed in Section IX, while the paper is concluded in Section X.

II. OBJECTIVE FUNCTION

The cost function based on net power, where the objective is to maximize the net power as proposed in [15], is given as

$$J = J_{\text{F}} - E - E_{\text{other}} = J_{\text{F}} - \int_0^T P(\mathbf{x}, \mathbf{u}) \, \mathrm{d}t - E_{\text{other}}(\mathbf{x}, t), \quad (1)$$

where E is the net energy of the system, $P(\mathbf{x}, \mathbf{u})$ is the system net power as a function of the system states $\mathbf{x}$ and inputs $\mathbf{u}$, and J_{F} is a cost imposed on the system final state. Note that (1) is formulated to fit into a minimization problem, meaning that the objective function is the negative of the desired maximization objective. $E_{\text{other}}(\mathbf{x}, t)$ is the energy used by subsystems other than the control actuators. The purpose of including $E_{\text{other}}(\mathbf{x}, t)$ in the cost function, possibly a function of the state and the time t, is to give the output of the optimization meaning when it comes to the total amount of power flowing in and out of the system. The net power function $P(\mathbf{x}, \mathbf{u})$, in its most general form, is given as

$$P(\mathbf{x}, \mathbf{u}) = s(\mathbf{x}) - m(\mathbf{x}, \mathbf{u}), \quad (2)$$

where $s(\mathbf{x})$ represents the solar power harvested by the system at the given state, while $m(\mathbf{x}, \mathbf{u})$ is the power used for actuation. The solar power function $s(\mathbf{x})$, defined as the sum of the power supplied by the solar panels, is given as

$$s(\mathbf{x}) = \eta_{\text{in}} \kappa(\mathbf{R}_b^i, \mathbf{r}_{\text{Sun}}) \delta(\mathbf{r}_{\text{Sun}}, \mathbf{r}_{\text{Earth}}), \quad (3)$$

where $\delta(\cdot, \cdot)$ quantifies the fraction of solar radiation that reaches the spacecraft, i.e. $\delta(\cdot, \cdot) = 1$ when the spacecraft is fully exposed to the Sun, and $\delta(\cdot, \cdot) = 0$ when the spacecraft is in the umbra region of the eclipse. Intermediate values correspond to the penumbra region. η_{in} represents the input efficiency of the batteries. The net power objective includes efficiency coefficients to model the cost of storing and using power and assumes that the power continuously cycles through the batteries. This assumption may cause the optimization to miss opportunities for direct consumption, making the results slightly pessimistic. The rotation matrix representation $\mathbf{R}_b^i$ represents the spacecraft's attitude. The indices i and b represent the Earth-centered inertial frame, referred to as the inertial frame, and the body frame, which is a body-fixed frame centered at the center of the spacecraft. $\mathbf{r}_{\text{Sun}}$ and $\mathbf{r}_{\text{Earth}}$ are vectors between the spacecraft and the Sun and the Earth, respectively. For spacecraft where the solar panels are flat, the amount of power the solar panels supply at a given attitude can be calculated as

$$\kappa(\mathbf{R}_b^i, \mathbf{r}_{\text{Sun}}) = \left(1 - \max\left((\hat{\mathbf{s}}^b)^{\mathsf{T}} \hat{\mathbf{n}}_k^b, 0\right)\right) \cdot$$
$$\sum_{j=1, j \neq k}^{n_s} \max\left((\hat{\mathbf{s}}^b)^{\mathsf{T}} \hat{\mathbf{n}}_j^b, 0\right) \left((\hat{\mathbf{s}}^b)^{\mathsf{T}} \hat{\mathbf{n}}_j^b\right) c_{s,j} A_j$$
$$+ \max\left((\hat{\mathbf{s}}^b)^{\mathsf{T}} \hat{\mathbf{n}}_k^b, 0\right) \left((\hat{\mathbf{s}}^b)^{\mathsf{T}} \hat{\mathbf{n}}_k^b\right) c_{s,k} A_k, \quad (4)$$

where n_s is the number of faces with solar panels, $\hat{\mathbf{s}}^b$ is the unit solar vector represented in the body frame, and $\hat{\mathbf{n}}_j^b$ is the normal vector of the jth solar panel pointing out of the body. $c_{s,j}$ is a constant that is the product of the solar irradiance and the solar panel efficiency, and A_j is the solar panel surface area of the jth face. This equation shows the particular case we are investigating in this paper, where one of the faces, denoted by index k, is assumed to entirely obscure the other faces of the spacecraft when it is exposed to solar irradiance. The implementation is handled by
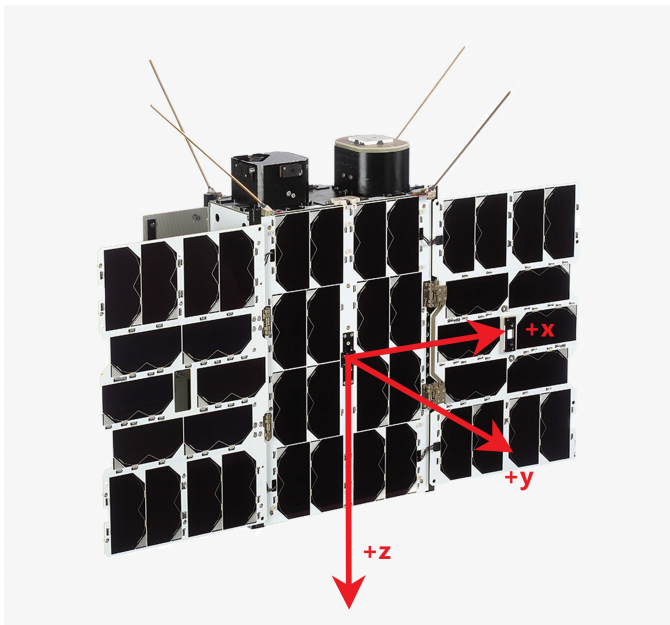
Fig. 1. Axes over a satellite of the same shape as HYPSO-2, showing the face with the deployable solar panels. The hyperspectral imager is mounted facing down in this image. Image credit: [21].
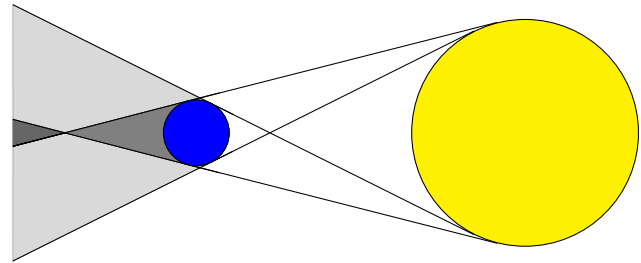

Fig. 2. Illustration showing the Earth and Sun with the umbra and penumbra regions. The penumbra are the areas in light gray to the left of the Earth (the blue circle), while the umbra region is the darker gray region enclosed by the two penumbra areas and the Earth. The dark gray triangle furthest left in the figure is the antumbra, which is not of interest to this application. Note that the distances in the figure are not to scale.

introducing a term that goes to zero whenever the obscuring face is exposed to solar irradiance, which is accomplished by the $\left(1 - \max\left(\left(\hat{\mathbf{s}}^b\right)^{\mathsf{T}} \hat{\mathbf{n}}_k^b, 0\right)\right)$ factor. The face in question in this paper is the large face with deployable solar panels that perfectly align with the rest of the satellite body, i.e., they form orthogonal angles with the other faces of the satellite frame. While this formulation is a simplification that only holds when the size of the solar panels goes to infinity or the size of the obscured faces goes to zero, it is assumed to be sufficient for our purposes, given that the deployable solar panels are relatively large compared to the faces they obscure. An example satellite, where this is valid, is the HYPSO-2 6U CubeSat depicted in Figure 1.

We use an approximation of the max$(\cdot)$ function, as in [15], implemented as

$$\max\left(x_1, x_2\right) = \frac{1}{2}\left(x_1 + x_2 + \sqrt{\left(x_1 - x_2\right)^2 + \alpha}\right), \quad (5)$$

where α is a small positive constant ensuring a smooth max function. With (5) being differentiable it is possible to take advantage of the automatic differentiation features of CasADi [20], and, more importantly, permits the use of a Newton-type solver like IPOPT.

The $\delta(\cdot, \cdot)$ function, a measure of how much sunlight reaches the spacecraft, can be defined by Algorithm 1. In defining the $\delta(\cdot, \cdot)$ function this way, we assume that the Sun and the Earth are spherical objects. In Algorithm 1, $\mathbf{r}_{\text{Sun}}$ is the vector from the spacecraft to the center of the Sun, $\mathbf{r}_{\text{Earth}}$ is the vector from the spacecraft to the center of the Earth, R_e is the radius of the Earth, and R_s is the radius of the Sun. As is shown in Fig. 2, the two spherical bodies' external and internal tangents intersect at two different points in space. These points are called external and internal homothetic centers, and their positions are defined by the position of the two spheres and

---

Algorithm 1 $\delta\left(\mathbf{r}_{\text{Sun}}, \mathbf{r}_{\text{Earth}}\right)$

$\mathbf{ES} \leftarrow \mathbf{r}_{\text{Sun}} - \mathbf{r}_{\text{Earth}}$
$\widehat{\mathbf{ES}} \leftarrow \frac{\mathbf{ES}}{\|\mathbf{ES}\|}$
$\cap_{\text{int}} \leftarrow \frac{R_e}{R_e + R_s} \mathbf{ES}$
$\cap_{\text{ext}} \leftarrow \frac{R_e}{R_e - R_s} \mathbf{ES}$
$\text{pos}_x \leftarrow \mathbf{r}_{\text{Earth}}^{\mathsf{T}} \widehat{\mathbf{ES}}$ ▷ Condition 1
$\alpha_{\text{int,cone}} \leftarrow \arcsin\left(\frac{R_e}{\|\cap_{\text{int}}\|}\right)$
$\text{adj}_{\text{int}} \leftarrow \frac{\mathbf{r}_{\text{Earth}}^{\mathsf{T}} \cap_{\text{int}}}{\cap_{\text{int}}^{\mathsf{T}} \cap_{\text{int}}} \cap_{\text{int}}$
$\text{hyp}_{\text{int}} \leftarrow \cap_{\text{int}} + \mathbf{r}_{\text{Earth}}$
$\alpha_{\text{int}} \leftarrow \arcsin\left(\frac{\|\text{hyp}_{\text{int}} \times \text{adj}_{\text{int}}\|}{\|\text{hyp}_{\text{int}}\| \|\text{adj}_{\text{int}}\|}\right)$
$\text{in}_{\text{int,cone}} \leftarrow |\alpha_{\text{int,cone}}| - |\alpha_{\text{int}}|$ ▷ Condition 2
$\alpha_{\text{ext,cone}} \leftarrow \arcsin\left(\frac{R_e}{\|\cap_{\text{ext}}\|}\right)$
$\text{adj}_{\text{ext}} \leftarrow \frac{\mathbf{r}_{\text{Earth}}^{\mathsf{T}} \cap_{\text{ext}}}{\cap_{\text{ext}}^{\mathsf{T}} \cap_{\text{ext}}} \cap_{\text{ext}}$
$\text{hyp}_{\text{ext}} \leftarrow \cap_{\text{ext}} + \mathbf{r}_{\text{Earth}}$
$\alpha_{\text{ext}} \leftarrow \arcsin\left(\frac{\|\text{hyp}_{\text{ext}} \times \text{adj}_{\text{ext}}\|}{\|\text{hyp}_{\text{ext}}\| \|\text{adj}_{\text{ext}}\|}\right)$
$\text{in}_{\text{ext,cone}} \leftarrow |\alpha_{\text{ext,cone}}| - |\alpha_{\text{ext}}|$ ▷ Condition 3
if $\text{pos}_x > 0$ **then**
    if $\text{in}_{\text{int,cone}} > 0$ **then**
        if $\text{in}_{\text{ext,cone}} > 0$ **then**
            $\delta \leftarrow \delta_{\text{umbra}}$ ▷ Umbra
        else if $\text{in}_{\text{ext,cone}} \leq 0$ **then**
            $\delta \leftarrow \delta_{\text{penumbra}}$ ▷ Penumbra
        end if
    else if $\text{in}_{\text{int,cone}} \leq 0$ **then**
        $\delta \leftarrow \delta_{\text{light}}$ ▷ Light
    end if
else if $\text{pos}_x \leq 0$ **then**
    $\delta \leftarrow \delta_{\text{light}}$ ▷ Light
end if
return δ

---

their radii. These intersection points, denoted using the symbol for intersection, $\cap$, in the algorithm, create conic sections together with the Earth, where the $\alpha_{\text{ext,cone}}$ and $\alpha_{\text{int,cone}}$ give the angle between the axes and the generatrix of the cones. These cones, where the internal cone is the cone defined by the intersection that lies between the Earth and the Sun and the Earth itself, and the outer cone, defined by the intersection on the far side of the Earth and the Earth, define the areas of space where the Earth cast a shadow. More precisely, if the spacecraft is inside the internal cone, meaning that the angle defined by α_{int} is smaller than $\alpha_{\text{int,cone}}$, then the spacecraft is in eclipse, but it might be in either the penumbra or the umbra regions. Similarly, the spacecraft is inside the external cone if α_{ext} is smaller than $\alpha_{\text{ext,cone}}$. If the spacecraft is in the outer and internal cones, it is in the umbra region. If it is in only the internal cone but not the outer cone, it is in one of the penumbra regions. These conditions are defined as condition 2 and condition 3 in Algorithm 1, respectively. The position argument, condition 1, is included so that only regions on the far side of the Earth, as seen from the Sun are considered. This is needed since it is possible to be inside the internal and the external cone while being between the Earth and the Sun, a region of space that obviously will be in the light. The algorithm serves the same purpose as the "Shadow" algorithm in [16].

As no external forces dependent on attitude are included in the orbit calculation, the $\delta(\cdot, \cdot)$ values can be calculated beforehand.

The shaded regions of the orbit eclipse, i.e. the penumbra, as seen in Fig. 2, do not all produce a complete shade. For a satellite orbiting the Earth in low-Earth orbit, there are three regions: the penumbra region, i.e., the semi-dark region enclosing the fully dark region, or the umbra, and the sunlit region of the orbit. Fig. 2 shows the various regions, but the scale of some of the elements in the illustration has been exaggerated in order to show the difference between the penumbra and the umbra regions. Due to the distance between the Sun and the Earth and the relatively short distance between the LEO (Low-Earth Orbit) spacecraft and the Earth, the spacecraft time in the penumbra region is short. Naturally, the time spent in the penumbra regions increases with the orbit's altitude, as can be seen from Fig. 2. While the penumbra region is distinctly separate from the sunlit and umbra regions [22], the amount of sunlight is not constant in the penumbra region. This could be modeled in Algorithm 1, under condition 2, as a gradual decrease as the spacecraft moves closer to the umbra region. For simplicity, the amount of sunlight in the penumbra region is defined as a fixed number between zero and one.

We assume an array of reaction wheels and magnetorquers, where only the reaction wheels are applied for attitude control of the spacecraft, while the magnetorquers are used to manage the momentum of the reaction wheels. For a spacecraft actuated by reaction wheels and magnetorquers, the actuation power $m(\mathbf{x}, \mathbf{u})$, where $\mathbf{x}$ is the state and $\mathbf{u}$ is the input, is the sum of the power usage for the reaction wheels $P_{\text{RW}}(\mathbf{x}, \mathbf{u})$
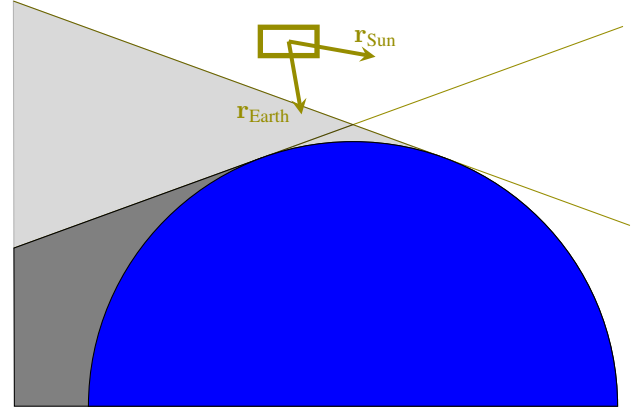

Fig. 3. Illustration showing a spacecraft in orbit with the umbra and (exaggerated) penumbra regions.

and the magnetorquers $P_{\text{mtq}}(\mathbf{u})$, or

$$
\begin{aligned}
m(\mathbf{x}, \mathbf{u}) &= P_{\text{RW}}(\mathbf{x}, \mathbf{u}) + P_{\text{mtq}}(\mathbf{u}) \\
&= \frac{1}{\eta_{rw}} |(\mathbf{A}\boldsymbol{\tau}_{\text{RW}}^w)^{\mathsf{T}} \mathbf{A}\boldsymbol{\omega}_{\text{RW}}^w| + \frac{1}{\eta_{\text{out}}} \left(\mathbf{I}_{\text{mtq}}^b\right)^{\mathsf{T}} \mathbf{V}_{\text{mtq}}^b,
\end{aligned}
\tag{6}
$$

where η_{rw} is the efficiency of the reaction wheels, and $\boldsymbol{\tau}_{\text{RW}}^w$ is the input torque represented in the wheel frame. η_{out} is the output efficiency of the batteries. $\boldsymbol{\omega}_{\text{RW}}^w$ is the angular velocity of the reaction wheels in the wheel frame, and $\mathbf{A}$ is the torque distribution matrix. The absolute value is included since energy only flows in one direction, from the batteries to the reaction wheels. In other words, it is assumed that the kinetic energy in the reaction wheels cannot be transformed into electrical energy in the batteries on board the spacecraft. $\mathbf{V}_{\text{mtq}}^b$ and $\mathbf{I}_{\text{mtq}}^b$ are vectors denoting the voltage over and current through the magnetorquers for each axis in the body frame. The power for the magnetorquers is included as they are part of the control system, even though they are not directly used for attitude control in this paper. For simplicity, the formula for the power used by magnetorquers is calculated by scaling the magnetic moment by its maximum value and multiplying it by the maximum power drawn by the magnetorquers:

$$
P_{\text{mtq}}(\mathbf{u}) = \frac{\sum\limits_{n=1}^{\infty} \left| m_{\text{mtq},i}^b \right|}{3 m_{\text{mtq, ub}}} P_{\text{mtq, max}},
\tag{7}
$$

where $m_{\text{mtq},i}^b$ is the i-th channel of the $\mathbf{m}_{\text{mtq}}$ vector, and the divisor the upper bound on the magnetic moment of the magnetorquers, $m_{\text{mtq, ub}}$, multiplied by three as the magnetorquers cover all three body frame axes. $\mathbf{m}_{\text{mtq}}$ is the magnetic moment of the magnetorquer, which is what is calculated by the control algorithm. $P_{\text{mtq, max}}$ is the maximum value for the power drawn by the magnetorquers. Thus, (6) in this paper takes the form

$$
\begin{aligned}
m(\mathbf{x}, \mathbf{u}) &= P_{\text{RW}}(\mathbf{x}, \mathbf{u}) + P_{\text{mtq}}(\mathbf{u}) \\
&= \frac{1}{\eta_{rw}} |(\mathbf{A}\boldsymbol{\tau}_{\text{RW}}^w)^{\mathsf{T}} \mathbf{A}\boldsymbol{\omega}_{\text{RW}}^w| + \frac{\sum\limits_{n=1}^{\infty} \left| m_{\text{mtq},i}^b \right|}{3 m_{\text{mtq, ub}}} P_{\text{mtq, max}}.
\end{aligned}
\tag{8}
$$

The output efficiency of the batteries is included in the value given to $P_{\text{mtq, max}}$.

The cost imposed on the problem relating to the final states of the system, J_F, can be chosen to be

$$
\begin{aligned}
J_F &= k_1 J_{\text{path,ref}} + k_2 J_{\text{velocity}} \\
&= k_1 \left(1 - \left| \left(\mathbf{q}_b^i \right)^\intercal \mathbf{q}_{\text{ref}} \right| \right) \\
&\quad + k_2 \left(\boldsymbol{\omega}_{\text{ref}}^b - \boldsymbol{\omega}_{ib}^b \right)^\intercal \left(\boldsymbol{\omega}_{\text{ref}}^b - \boldsymbol{\omega}_{ib}^b \right),
\end{aligned}
\tag{9}
$$

where $J_{\text{path,ref}}$ is a metric on SO(3) [23] that denotes the cost of not reaching the desired attitude, J_{velocity} is the cost of not reaching the desired final angular velocity, and k_1 and k_2 are weights. $\mathbf{q}_{\text{ref}}$ and $\boldsymbol{\omega}_{\text{ref}}^b$ are the reference values for the attitude quaternion and the angular velocity, respectively. $J_{\text{path,ref}}$ is implemented using the smooth max function (5),

$$
\left| \left(\mathbf{q}_b^i \right)^\intercal \mathbf{q}_{\text{ref}} \right| = \max \left(\left(\mathbf{q}_b^i \right)^\intercal \mathbf{q}_{\text{ref}}, - \left(\mathbf{q}_b^i \right)^\intercal \mathbf{q}_{\text{ref}} \right).
\tag{10}
$$

With J_F defined this way, the problem becomes multi-objective because the cost function weights energy usage against reference tracking.

III. OPTIMAL CONTROL PROBLEM

The general optimal control problem, based on (1), is defined as

$$
\min_{\mathbf{x}, \mathbf{u}} \quad J_F - \int_0^T P(\mathbf{x}, \mathbf{u}) \, \mathrm{d}t - E_{\text{other}}(\mathbf{x}, t)
\tag{11a}
$$

$$
\text{s.t. } \dot{\mathbf{x}} = \mathbf{f}(\mathbf{x}, \mathbf{u})
\tag{11b}
$$

$$
\mathbf{g}(\mathbf{x}) \leq 0
\tag{11c}
$$

$$
\mathbf{u}_{\text{lb}} \leq \mathbf{u} \leq \mathbf{u}_{\text{ub}}
\tag{11d}
$$

$$
\mathbf{x}(0) = \mathbf{x}_0,
\tag{11e}
$$

where the net energy objective function is constrained by the system dynamics in (11b). T is the length of the control horizon. The $\mathbf{g}(\mathbf{x})$ vector constrains the state vector $\mathbf{x}$ to some bounds, such as upper and lower bounds on reaction wheel angular velocities. The control input $\mathbf{u}$ is bounded by both lower bounds, $\mathbf{u}_{\text{lb}}$, and upper bounds, $\mathbf{u}_{\text{ub}}$. We use the J_F term to drive the state variables to the desired final states. Note that the problem appears to be singular.

Defining the state $\mathbf{x} = \left[\left(\mathbf{q}_b^i \right)^\intercal, \left(\boldsymbol{\omega}_{ib}^b \right)^\intercal, \left(\boldsymbol{\omega}_{\text{RW}}^w \right)^\intercal \right]^\intercal$ and the input $\mathbf{u} = \left[\left(\boldsymbol{\tau}_{\text{RW}}^w \right)^\intercal, \left(\boldsymbol{\tau}_{\text{mtq}}^b \right)^\intercal \right]^\intercal$, the optimal control problem is defined by [18]

$$
\min_{\mathbf{x}, \mathbf{u}} \quad J_F - \int_0^T P(\mathbf{x}, \mathbf{u}) \, \mathrm{d}t - E_{\text{other}}(\mathbf{x}, t)
\tag{12a}
$$

$$
\text{s.t. } \dot{\mathbf{q}}_b^i = \frac{1}{2} \mathbf{T}(\mathbf{q}_b^i) \boldsymbol{\omega}_{ib}^b + \frac{1}{2} \rho \mathbf{q}_b^i \left(\left(\left(\mathbf{q}_b^i \right)^\intercal \mathbf{q}_b^i \right)^{-1} - 1 \right)
\tag{12b}
$$

$$
\frac{^b d}{dt} \boldsymbol{\omega}_{ib}^b = \mathbf{J}_s^{-1} \big(-\mathbf{S}\left(\boldsymbol{\omega}_{ib}^b \right) \left(\mathbf{J} \boldsymbol{\omega}_{ib}^b + \mathbf{A} \mathbf{J}_w \boldsymbol{\omega}_{\text{RW}}^w \right) - \mathbf{A} \boldsymbol{\tau}_{\text{RW}}^w
$$
$$
+ \boldsymbol{\tau}_{\text{mtq}}^b + \boldsymbol{\tau}_{\text{ext}}^b \big)
\tag{12c}
$$

$$
\frac{^w d}{dt} \boldsymbol{\omega}_{\text{RW}}^w = \mathbf{J}_w^{-1} \boldsymbol{\tau}_{\text{RW}}^w - \mathbf{A}^\intercal \frac{^b d}{dt} \boldsymbol{\omega}_{ib}^b
\tag{12d}
$$

$$
\frac{^i d}{dt} \mathbf{r}^i = \mathbf{v}^i
\tag{12e}
$$

$$
\frac{^i d}{dt} \mathbf{v}^i = -\frac{\mu \mathbf{r}^i}{\| \mathbf{r}^i \|^3}
\tag{12f}
$$

$$
\boldsymbol{\tau}_{\text{RW,lb}}^w \leq \boldsymbol{\tau}_{\text{RW}}^w \leq \boldsymbol{\tau}_{\text{RW,ub}}^w
\tag{12g}
$$

$$
\mathbf{x}(0) = \mathbf{x}_0,
\tag{12h}
$$

where (12b) describes the kinematics of the system, and (12c) and (12d) describe the dynamics of the spacecraft and the reaction wheels, respectively [18]. The model assumes that the spacecraft is a rigid body, where the translational motion is described in (12e) and (12f). $\mathbf{q}_b^i = [\eta_b^i, (\boldsymbol{\epsilon}_b^i)^\intercal]^\intercal$ is the attitude unit quaternion, where η_b^i is the scalar and $\boldsymbol{\epsilon}_b^i$ is the vector part of the quaternion. Note that the quaternion $\mathbf{q}_b^i$ defines the rotation matrix in (3) and (4). In the case study, one reaction wheel exists for each of the body frame axes, in addition to a fourth reaction wheel with equal capacity along each body frame axis. This leads to the torque distribution matrix $\mathbf{A}$ that gives the mapping between the wheel frame and the body frame:

$$
\mathbf{A} = \frac{1}{3} \begin{bmatrix} 1 & 0 & 0 & \sqrt{3} \\ 0 & 1 & 0 & \sqrt{3} \\ 0 & 0 & 1 & \sqrt{3} \end{bmatrix}.
\tag{13}
$$

The inertia matrices $\mathbf{J}_s$, $\mathbf{J}_w$, and $\mathbf{J} = \mathbf{J}_s + \mathbf{A} \mathbf{J}_w \mathbf{A}^\intercal$ represent the inertia of the spacecraft only, the reaction wheels, and the total inertia of the complete spacecraft, respectively. μ is the standard gravitational parameter of the Earth, and m is the spacecraft's mass. The external torques that act on the spacecraft are represented by $\boldsymbol{\tau}_{\text{ext}}^b$, and $\boldsymbol{\tau}_{\text{RW,lb}}^b$ and $\boldsymbol{\tau}_{\text{RW,ub}}^b$ are the lower and upper bound on the reaction wheel torques, respectively. The environmental torques are defined in Appendix A. The limits are defined similarly for the torque from the magnetorquers, $\boldsymbol{\tau}_{\text{mtq}}^b$, but the magnetorquer limits are not included in the optimal control problem since the optimal solver does not determine the magnetic torque. The angular velocity of the reaction wheels is given by $\boldsymbol{\omega}_{\text{RW}}^w$. Note that the angular velocity of the reaction wheels has superscript w. This denotes a wheel frame, which has a channel for each reaction wheel, and thus, the vectors in this frame have the same dimension as the number of reaction wheels. Since the reaction wheels only rotate about one axis, the wheel frame does not rotate relative to the body frame. The $\mathbf{T}(\mathbf{q})$ matrix is given by [24]

$$
\mathbf{T}(\mathbf{q}) = \begin{bmatrix} -\boldsymbol{\epsilon}^\intercal \\ \eta \mathbf{I}_{3\times3} + \mathbf{S}(\boldsymbol{\epsilon}) \end{bmatrix},
\tag{14}
$$

This article has been accepted for publication in IEEE Transactions on Control Systems Technology. This is the author's version which has not been fully edited and content may change prior to final publication. Citation information: DOI 10.1109/TCST.2024.3356392

6

where $\mathbf{I}_{3x3}$ is the three-dimensional identity matrix and $\mathbf{S}(\cdot)$ is a skew-symmetric matrix corresponding to the vector cross product in three dimensions.

The position of the satellite in Earth-centered inertial frame is given as $\mathbf{r}^i$. This vector is denoted $\mathbf{v}^i$ in Fig. 3. The corresponding velocity is given by $\mathbf{v}^i$, and μ is the standard gravitational parameter of the Earth.

The unit quaternion is not constrained by a normalization constraint other than that the initial attitude should be a unit quaternion. The norm of the unit quaternion is preserved through the accuracy of the numerical integrator and the Baumgarte stabilization term $\frac{1}{2}\rho\mathbf{q}\left((\mathbf{q}^\mathsf{T}\mathbf{q})^{-1} - 1\right)$, where ρ is a small positive constant [25].

IV. Magnetorquers control

The magnetorquers are only used for momentum management of the reaction wheels, with the control algorithm given as [26]

$$\boldsymbol{\tau}_{\text{mtq}} = \mathbf{S}(\mathbf{m}^b)\mathbf{B}^b = \mathbf{S}\left(\frac{k_m}{\|\mathbf{B}^b\|_2}\left(\mathbf{S}\left(\mathbf{h}_e^b\right)\mathbf{B}^b\right)\right)\mathbf{B}^b, \quad (15)$$

where $\mathbf{m}^b$ is the magnetic moment produced by the magnetorquers. k_m is a positive constant, and $\mathbf{h}_e^b$ is the error in angular momentum for the reaction wheels, given as

$$\mathbf{h}_e^b = \mathbf{A}\mathbf{J}_w(\boldsymbol{\omega}_{\text{RW,ref}}^w - \boldsymbol{\omega}_{\text{RW}}^w), \quad (16)$$

where reference angular velocity of the reaction wheels is denoted as $\boldsymbol{\omega}_{\text{RW,ref}}^w$. The commanded torque to the magnetorquers is to produce is calculated directly in this paper using (15) and (16). Using the reaction wheels and the magnetorquers this way is in line with the design choices made for the HYPSO-2 mission, which is used for the simulation case study in this paper.

V. Optimization and initial guesses

The optimal control problem is solved using the IPOPT solver [27] in CasADi, where the optimal control problem in (12) is discretized as a multiple-shooting problem. The dynamics are discretized and integrated using the CasADi built-in implementation of the Runge-Kutta 4 integrator.

This paper uses a PD controller to produce the initial guesses for the optimal control problem in (12) by pointing the spacecraft toward an optimal solar power reference. The PD controller is also used as a benchmark for the optimal control solution, i.e., to evaluate the improvements achieved by the optimization. The PD controller formulation is based on quaternions, given by [1]

$$\boldsymbol{\tau}_{\text{RW}}^b = \mathbf{K}_p\boldsymbol{\epsilon}_e - \mathbf{K}_d\left(\boldsymbol{\omega}_{ib,\text{ref}}^b - \boldsymbol{\omega}_{ib}^b\right), \quad (17)$$

where $\mathbf{K}_d > 0$, $\mathbf{K}_p > 0$ are constant controller gain matrices, $\boldsymbol{\omega}_{ib,\text{ref}}^b$ is the reference angular velocity, and $\boldsymbol{\epsilon}_e$ is the error in the vector part of the quaternion, given as the final three elements of $\mathbf{q}_e = \mathbf{q}_d^{-1}\otimes\mathbf{q}$, where $\mathbf{q}_d$ is the desired quaternion and $\otimes$ is the Hamilton product.

The quaternion references for the PD controller are set to the attitude with the maximal incoming solar energy at the beginning of the time horizon, then to the final reference quaternion towards the end. The attitude with the maximal incoming solar power is found by minimizing the incoming power function $\kappa(\cdot)$, from (4), with respect to the attitude, here represented by the attitude unit quaternion $\mathbf{q}$,

$$\min_{\mathbf{q}} \; -\kappa(\mathbf{q})^2 + k_{\max}J_{\text{path}}(\mathbf{q}) \quad (18\text{a})$$

$$\text{s.t. } \mathbf{q}^\mathsf{T}\mathbf{q} = 1, \quad (18\text{b})$$

where k_{max} is a positive constant, and J_{path} is a cost introduced to ensure that only one attitude would be optimal. J_{path} is defined as [23]

$$J_{\text{path}}(\mathbf{q}) = 1 - |\mathbf{q}^\mathsf{T}\mathbf{q}_{\text{ref}}|, \quad (19)$$

where $\mathbf{q}_{\text{ref}}$ is the reference attitude quaternion. The absolute value is implemented using the smooth max function defined in (5), with $|\mathbf{q}^\mathsf{T}\mathbf{q}_{\text{ref}}| = \max(\mathbf{q}^\mathsf{T}\mathbf{q}_{\text{ref}}, \text{-}\mathbf{q}^\mathsf{T}\mathbf{q}_{\text{ref}})$. Note that the metric used in J_{path} does not differentiate between the positive and negative inner product. Thus, the distance between the reference quaternion and the positive and the negative quaternion will be the same. The J_{path} term is only meant to differentiate between attitudes; several attitudes would otherwise be optimal, so k_{max} should be small. The scenario of several optimal attitudes is not unlikely: Using a CubeSat with only one solar panel on one side as an example, it is trivial to see that it would be optimal to point the axis with the solar panel towards the sun vector, but any rotation about this axis would result in the same optimal solar power.

The net power cost function appears singular, and singular control problems can be challenging in the discretization phase. However, note that we do not use regularization in the optimal control problem formulation in (12) as the solver finds solutions without it.

VI. Control scenario

The case study is based on the HYPSO satellites' concept of operations, [17, Table VII], where the satellite makes a slewing maneuver during imaging, see Fig. 4. This is a maneuver with a constant angular velocity, about the satellite's y-axis during image acquisition. The control task will include a sequence of image captures within a single pass. The allocated time for the various parts of the tasks are shown in Table I. In particular, we will study the HYPSO-2 satellite which differs from HYPSO-1 by having deployable solar panels and an X-band radio communication downlink with significantly increased link capacity when compared to HYPSO-1's S-band radio downlink. A typical image taken by the hyperspectral camera is 85 MB, and the X-band is assumed to give a datarate of 10 Mbps, which means that a full hyperspectral image can be downlinked in 68 seconds.

The full scenario is modeled as a series of smaller optimizations for each of the tasks as opposed to one large optimization, which it should be noted is not necessarily optimal in a mathematically rigorous sense.

The optimizations described in this paper occur between image acquisitions or downlinks. The maneuver during image acquisition is not the subject matter of this paper and is thus
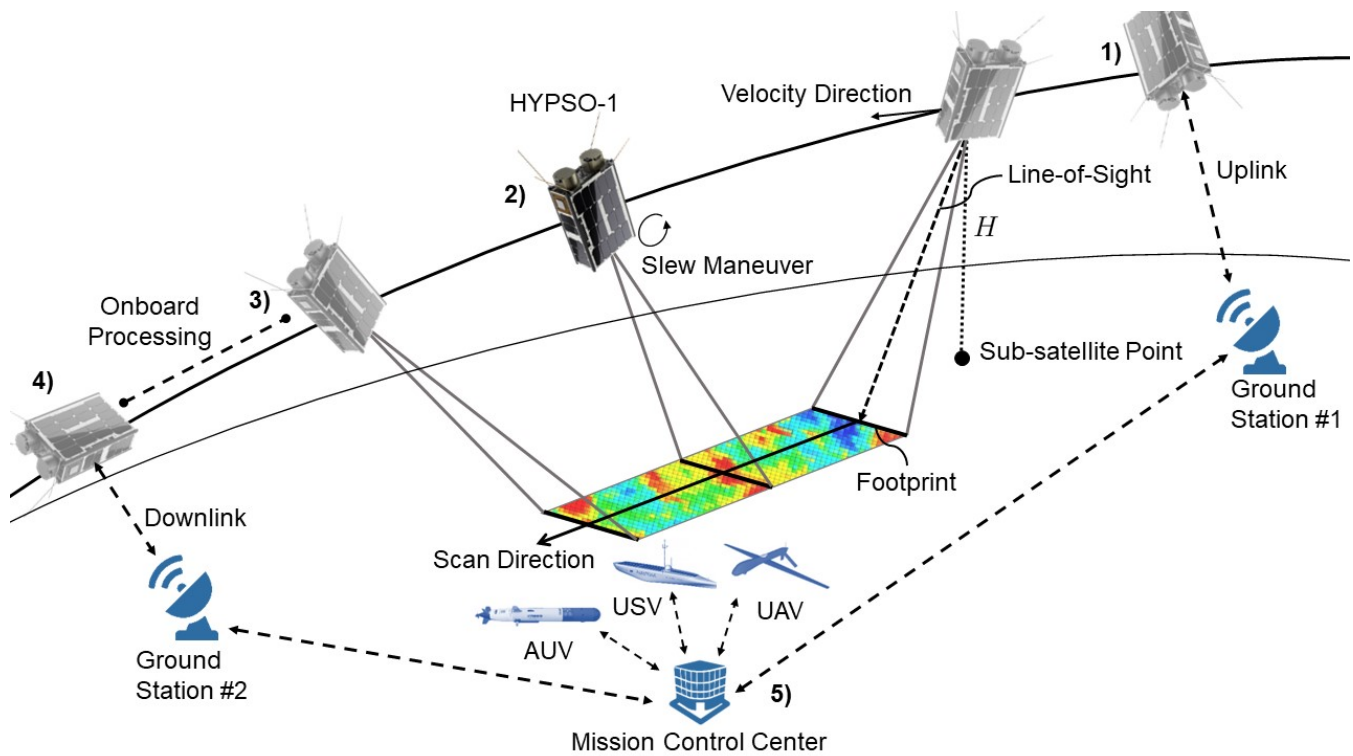
This article has been accepted for publication in IEEE Transactions on Control Systems Technology. This is the author's version which has not been fully edited and content may change prior to final publication. Citation information: DOI 10.1109/TCST.2024.3356392

7

Fig. 4. Concept of operations (CONOPS) for the HYPSO satellites, from [17].

omitted. The image acquisition is accomplished in simulation by integrating the translational variables over the stated duration while keeping the other attitude constant. The difference between image capture maneuvers and downlink maneuvers is that the optimization leading up to the image acquisitions should go towards a non-zero angular velocity reference, whereas zero is given as the angular velocity reference for the downlink maneuvers. Additionally, the satellite is rotated differently for the downlink maneuvers, as the antenna and the camera are not placed on the same face. The longest idle phase spans the eclipse from Nigeria to Svalbard (optimization task 7). There are no image acquisitions during the eclipse since the HYPSO-2 imager payload, the hyperspectral camera, requires the target to be lit to produce good data.

The reference quaternions are chosen to coincide with the various targets in Fig. 5, while the angular velocity references depend on whether their target is for imaging or downlinking data. The angular velocity reference is zero for downlinking data since the radio antennas have relatively wide beams. In contrast, it is set to a fixed angular velocity about the body frame y-axis for optimizations that transition into an image acquisition: this way, the slewing maneuver the satellite performs during imaging can be prepared directly from the optimization. The targets/tasks coincide with current areas of interest for the HYPSO mission. The map also shows the position and ground track of the HYPSO-1 satellite on the day used for this paper. The references are inferred from the outputs from an internally developed software suite for satellite operations at NTNU. The attitude and angular velocity references are in Table II.

Fig. 5. Map showing the position and ground track of HYPSO-1 as of March 14, 2023. A dark yellow circle marks the satellite, and the satellite ground track is marked in red. The initial target, Svalbard, and the final target, KSAT Spain, are marked by dark red crosses. The other targets are marked with yellow crosses following the satellite's path, going from North to South. The satellite is close to the 6th target in the figure, the Nigerian coastline.

VII. Simulation setup

The optimal trajectories are calculated once. The output from the sun-pointing PD controller from Section V is used as the initial values for the optimization. The PD controller makes the satellite point towards what it perceives as the optimal sun-pointing attitude, given by (18), until 20 seconds before the satellite's new target reference is used for the attitude and angular rate. The PD controller is constrained similarly to the optimal control problem in (12). The PD controller that provides the initial values and the optimal control problem has a discretization step size h of 2 seconds. The total length of the maneuvers, from start to finish, is 5580 seconds or 93 minutes. During this time, the satellite goes through more than a complete orbit, meaning that the satellite spends some time in the light and some in the shade, and thus $\delta(\cdot, \cdot)$ varies between 0 and 1.

The parameters used in the simulation can be seen in Table III. Note that the constant $c_{s,j}$ from (4), given by the solar irradiance multiplied by the given solar panel's efficiency, is equal to c_s in this simulation as all the solar panels are assumed to be identical.

TABLE I
OPTIMIZATION SCENARIO FOR HYPSO-2

Task	Start time (UTC)	End time (UTC)	Duration (s)
Solar energy harvesting, Optimization task 1	09:31:11	09:32:51	100
Communication, Svalbard, Norway	09:32:51	09:34:51	120
Solar energy harvesting, Optimization task 2	09:34:51	09:35:31	40
Image acquisition, Finnmark, Norway	09:35:31	09:36:31	60
Solar energy harvesting, Optimization task 3	09:36:31	09:37:31	60
Image acquisition, Frohavet, Norway	09:37:31	09:38:31	60
Solar energy harvesting, Optimization task 4	09:38:31	09:38:51	20
Image acquisition, Mjøsa, Norway	09:38:51	09:39:51	60
Solar energy harvesting, Optimization task 5	09:39:51	09:45:01	310
Communication, KSAT Spain, Spain	09:45:01	09:46:33	92
Solar energy harvesting, Optimization task 6	09:46:33	09:53:01	388
Image acquisition of coastline, Nigeria	09:53:01	09:54:01	60
Solar energy harvesting, Optimization task 7	09:54:01	11:07:01	4 380
Communication, Svalbard, Norway	11:07:01	11:10:01	180
Solar energy harvesting, Optimization task 8	11:10:01	11:10:41	40
Image acquisition, Finnmark, Norway	11:10:41	11:11:41	60
Solar energy harvesting, Optimization task 9	11:11:41	11:12:41	60
Image acquisition, Trondheim, Norway	11:12:41	11:13:41	60
Solar energy harvesting, Optimization task 10	11:13:41	11:18:45	304
Communication, KSAT Spain, Spain	11:18:45	11:20:47	122

TABLE III
OPTIMIZATION CONSTANTS

Variable	Value	Unit
Step size (h)	2	s
Solar irradiance	1366	W/m^2
Solar panel efficiency	20	%
c_s	272.2	W/m^2
η_{rw}	0.85	-
α	10^{-5}	-
$k_{\max}$	1	W^2
k_1	$T \cdot 1.75 \cdot 10^2$	W
k_2	$T \cdot 10^4$	W $\cdot$ s^2
ρ	$1.1 \cdot 10^{-2}$	-
$\boldsymbol{\tau}^b_{\mathrm{RW,lb}}$	$-3.2 \cdot 10^{-3}$	N·m
$\boldsymbol{\tau}^b_{\mathrm{RW,ub}}$	$3.2 \cdot 10^{-3}$	N·m

The inertia matrices are given by

$$\mathbf{J} = \begin{bmatrix} 0.0950 & 0.0000 & 0.0010 \\ 0.0000 & 0.1370 & 0.0000 \\ 0.0010 & 0.0000 & 0.0570 \end{bmatrix} \mathrm{kg} \cdot \mathrm{m}^2, \quad \mathbf{J}_w = I_w \mathbf{I}_{4\mathrm{x}4},$$

(20)

where $I_w = 2.1 \cdot 10^{-4}$ kg·m^2. Note that not all the sides of the 6U satellite are covered in solar panels. The areas of the solar cell covered surfaces A_j are then the entries in the vector A in (21),

$$A = [0.024, 0.144, 0, 0.024, 0.048, 0] \mathrm{\ m}^2. \quad (21)$$

The deployable solar panels are on the positive y-face of the body frame, indicated by the largest entry in the A vector in (21).

The position of the Sun relative to the Earth is given in the Earth-centered inertial frame as $\mathbf{r}^i_{\mathrm{Sun\text{-}Earth}} = 1.49599870 \cdot 10^{11} [0.8944, 0, 0.4472]^\mathsf{T}$ m and is constant throughout the simulation. This is assumed to be sufficient due to the simulation's relatively short duration relative to the rotation of the Earth-centered inertial frame around the Sun. $\hat{\mathbf{s}}^b$, which is used

TABLE II
CONTROL REFERENCES FOR THE TASKS IN TABLE I

Target	$\mathbf{q}_{\mathrm{ref}}$	$\boldsymbol{\omega}^b_{ib,\mathrm{ref}}(°/\mathrm{s})$
Svalbard, Norway (1)	[.853, .372, -.019, -.366]$^\mathsf{T}$	$[0, 0, 0]^\mathsf{T}$
Finnmark, Norway (2)	[.084, .918, -.329, -.205]$^\mathsf{T}$	$[0, -0.754, 0]^\mathsf{T}$
Frohavet, Norway (3)	[.297, -.858, .407, .102]$^\mathsf{T}$	$[0, -0.754, 0]^\mathsf{T}$
Mjøsa, Norway (4)	[.275, .860, -.262, -.343]$^\mathsf{T}$	$[0, -0.754, 0]^\mathsf{T}$
KSAT Spain, Spain (5)	[.827, .123, .333, -.435]$^\mathsf{T}$	$[0, 0, 0]^\mathsf{T}$
Coastline, Nigeria (6)	[.034, .710, .474, .519]$^\mathsf{T}$	$[0, -0.754, 0]^\mathsf{T}$
Svalbard, Norway (7)	[.677, .642, -.151, -.327]$^\mathsf{T}$	$[0, 0, 0]^\mathsf{T}$
Finnmark, Norway (8)	[.405, -.835, .372, -.018]$^\mathsf{T}$	$[0, -0.754, 0]^\mathsf{T}$
Trondheim, Norway (9)	[.389, -.828, .402, .036]$^\mathsf{T}$	$[0, -0.754, 0]^\mathsf{T}$
KSAT Spain, Spain (10)	[.223, .906, -.304, -.195]$^\mathsf{T}$	$[0, 0, 0]^\mathsf{T}$

for (4), is found by transforming $\mathbf{r}_{\text{Sun}}^i = \mathbf{r}_{\text{Sun-Earth}}^i + \mathbf{r}^i$ to the body frame after normalizing the vector.

The initial conditions for the satellite before the first optimization are $\mathbf{x}_0 = \left[\mathbf{q}_b^i(0); \boldsymbol{\omega}_{ib}^b(0); \boldsymbol{\omega}_{\text{RW}}^b(0)\right] = [0, 0, 1, 0, \text{-}0.01, 0.02, 0.01, 209.4, 209.4, 209.4, -362.8]^{\mathsf{T}}$, and for optimization 2 through 9, the initial values are taken from the satellite maneuver that leads up to the optimization. The initial values for $\boldsymbol{\omega}_{ib}^b$ are given in rad/s. The reference for the angular velocity of the reaction wheels is the same as the initial value, which means $[209.4, 209.4, 209.4, -362.8]^{\mathsf{T}}$, all in rad/s. The quaternion and angular velocity references are in Table II.

The torque from the sun-pointing PD controller used to find the initial values for the optimization is constrained by the same bounds as the optimal control torque. The PD controller gains $\mathbf{K}_p$ and $\mathbf{K}_d$ with the constant values $1 \cdot 10^{-2}$ and $3.56 \cdot 10^{-2}$, respectively, are found through tuning.

The magnetic field is modeled using the IGRF model, defined by the potential function [28]. An adaptation of the implementation presented in [29] is used.

The value for the other loads in the cost function, $E_{\text{other}}(\mathbf{x}, t)$, are estimated based on a preliminary mission analysis. When harvesting solar power, the term is set to -13.5 W. The cost during imaging is -29.5 W, and during communication with a ground station, it is -40 W.

The external torques, $\boldsymbol{\tau}_{\text{ext}}^b$, that are included are detailed in Appendix A. Any other effects in the actuators that have not previously been mentioned, such as handling dead zones in reaction wheels or other nonlinear effects, are not included in the simulations and are then, in effect, assumed to be handled by a lower-level control layer. Depth-of-discharge is not considered in this article, so the capacity of the batteries is not modeled.

Table IV gives the initial orbital elements. The other parameters used for the simulation are shown in Table V.

TABLE IV
ORBITAL ELEMENTS

Variable	Value	Unit
Semimajor axis	6905.1	km
Eccentricity	0.0007757	-
Inclination	97.439	°
Right ascension of the ascending node	139.3136	°
Argument of perigee	213.7547	°
True anomaly	54	°

VIII. RESULTS

Fig. 6 shows the optimal attitude quaternion trajectory $\mathbf{q}_b^i$ resulting from IPOPT solving the optimal control problem in (12) for all references detailed in Table I and Table II. All the figures have vertical lines which mark the start of each of the optimization tasks. The grey-shaded region indicates that the satellite is in eclipse, for a few seconds in the penumbra and then in the umbra. The satellite rotates from in the shadow, a rotation which is owing to the torques from the environment, see Fig. 16, and a few features of the solution produced by the optimal solver are detailed in the discussion section. Fig. 7

TABLE V
SIMULATION PARAMETERS

Variable	Value	Unit
δ_{light}	1	-
δ_{penumbra}	0.2	-
δ_{umbra}	0	-
Mass, satellite (m)	7	kg
μ	$3.986 \cdot 10^{14}$	-
Radius, Earth	$6.371 \cdot 10^6$	m
Radius, Sun	$6.96340 \cdot 10^8$	m
$m_{\text{mtq,lb}}^b$	-0.34	A·m^2
$m_{\text{mtq,ub}}^b$	0.34	A·m^2
Residual magnetic dipole ($\mathbf{m}_{\text{res}}^b$)	$12[1, 1, 1]^{\mathsf{T}}$	mA·m^2
k_{eddy}	0.01	-
η_{in}	0.92	-
$P_{\text{mtq, max}}$	2.52	W

shows how the net power cost function, (1), evolves over the control horizon. The figure shows that the net power is reduced to around zero when entering the umbra. The penumbra region, where the net power supplied to the spacecraft is significantly reduced, but not to zero, is not visible in the figure as the penumbra only spans some seconds with the low altitude orbit of HYPSO-2. This is expected behavior, as only a percentage of the light from the Sun reaches the satellite in the penumbra region, and nothing does while it is in the umbra region. The amount of sunlight that reaches the satellite during the simulation, defined by the $\delta(\cdot, \cdot)$ function, can be seen in Fig. 8. The satellite spends about 20 seconds in the penumbra region in this scenario. The solar power function, (4), over time, is shown in Fig. 9. This figure clearly illustrates the need for a $\delta(\cdot, \cdot)$ part in the net power cost function, as there will be no solar power moving in to the satellite while it is in the umbra region. Following this argument, it is intuitive that close to zero net power is optimal during the umbra region, as the optimal control problem reduces to minimizing the actuation power in (6). In Fig. 10, this is accomplished during the umbra region for this control scenario. Fig. 10 has two peaks for each optimization: one at the beginning and one at the end. These peaks coincide with the net energy cost function Fig. 7, going from the initial sub-optimal solar power attitude to an optimal one at first and from the optimal attitude to the final attitude. A direct result of these peaks, the satellite's angular velocity, is shown in Fig. 12. The cumulative net power over time, giving the total energy accumulated by the system over the control horizon, is given in Fig. 11. The figure also includes the performance of the PD controller. Fig. 13 displays the torques from the reaction wheels. This figure is closely related to Fig. 10, but it is possible to see that some smaller torque is applied to the reaction wheels also inside the umbra region. This behavior is also displayed in the figure showing the satellite's angular velocity, Fig. 12. The reaction wheels' angular velocity can be seen in Fig. 14. The torque from the magnetorquers is shown in Fig. 15, while the perturbing torques are shown in Fig. 16. The small breaks where the different plots flatline, such as the torque from the reaction wheels in Fig. 13, often coincide with different

This article has been accepted for publication in IEEE Transactions on Control Systems Technology. This is the author's version which has not been fully edited and content may change prior to final publication. Citation information: DOI 10.1109/TCST.2024.3356392

10

imaging slewing maneuvers and downlink communication pointing maneuvers.

The computation time of the given control scenario is shown in Table VI for each of the individual optimization tasks. The optimizations were performed with a 2.4 GHz 8-core processor. The power gained over time, or the energy gained, by the different control schemes, evaluated by using the cost function in (2), is shown in Table VII. The optimal solver finds a solution that returns 3229 J more than the PD controller alternative, giving an increase of 11.3%. The table also shows the increase provided by the optimal solution compared to the PD controller when the scenario is reduced, such as without including imaging and communication, without including the energy spent on the other subsystems, and an example where the longest optimization is omitted.

The values for other objectives, the regulation towards the quaternion and angular velocity references, are shown in Table VIII. The error values are given by the equation shown in (9), meaning that the quaternion error is given by $\left(1 - \left|\left(\mathbf{q}_b^i\right)^\mathsf{T}\mathbf{q}_{\text{ref}}\right|\right)$, and the angular velocity error is given by $\left(\boldsymbol{\omega}_{\text{ref}}^b - \boldsymbol{\omega}_{ib}^b\right)^\mathsf{T}\left(\boldsymbol{\omega}_{\text{ref}}^b - \boldsymbol{\omega}_{ib}^b\right)$. Two of the quaternion error values are negative only due to the change in approximated absolute value function that is used. The table shows that the optimal solver drives values significantly closer to the references than the PD controller.

TABLE VI
IPOPT OUTPUT

Optimization task number	Number of iterations	Total CPU secs in IPOPT (w/o function evaluations)	Total CPU secs in NLP function evaluations
1	106	2.093	38.429
2	81	0.535	12.023
3	119	0.997	26.306
4	27	0.141	2.014
5	402	13.459	457.596
6	198	8.195	289.489
7	253	130.876	4323.100
8	177	1.432	27.125
9	89	0.879	20.079
10	1064	39.577	1226.046

TABLE VII
ENERGY, COMPARISON

Optimization task number	Energy, optimal (J)	Energy, PD (J)	Energy, increase (J)	Energy, increase, (%)
1	2 080.3	1 849.0	+231.3	+12.5
2	726.6	365.0	+361.6	+99.1
3	931.8	567.4	+364.4	+64.2
4	81.3	-18.8	+100.1	-
5	6 788.5	6 507.5	+280.9	+4.32
6	8 490.7	8 241.7	+249.0	+3.02
7	25 825.9	25 539.8	+286.0	+1.12
8	498.5	131.8	+366.7	+278
9	893.2	469.3	+423.9	+90.3
10	6 503.5	5 938.8	+564.7	+9.51
Total energy	31 892	28 663	+3 229	+11.3
Total energy without imaging and comms	52 844	49 615	+3 229	+6.51
Net energy without imaging and comms	129 794	126 565	+3 229	+2.55
Total energy, excluding task 7	10 350	7 407	+2 943	+39.7
Total energy without imaging and comms, excluding task 7	27 019	24 076	+2 943	+12.3
Net energy without imaging and comms, excluding task 7	44 839	41 895	+2 943	+7.02

TABLE VIII
REFERENCE COMPARISON

Task number	Quaternion error, optimal	Quaternion error, PD	Angular velocity error, optimal	Angular velocity error, PD
1	$4.2744 \cdot 10^{-6}$	$4.8769 \cdot 10^{-4}$	$8.7045 \cdot 10^{-10}$	$1.3583 \cdot 10^{-3}$
2	$8.1493 \cdot 10^{-5}$	$5.0495 \cdot 10^{-5}$	$5.3019 \cdot 10^{-8}$	$2.6908 \cdot 10^{-4}$
3	$1.1256 \cdot 10^{-5}$	$3.5457 \cdot 10^{-3}$	$1.2866 \cdot 10^{-8}$	$1.5230 \cdot 10^{-3}$
4	$7.2804 \cdot 10^{-4}$	$1.2148 \cdot 10^{-1}$	$3.8977 \cdot 10^{-7}$	$3.9212 \cdot 10^{-2}$
5	$1.3382 \cdot 10^{-6}$	$2.8139 \cdot 10^{-5}$	$5.9935 \cdot 10^{-10}$	$2.9088 \cdot 10^{-6}$
6	$4.8979 \cdot 10^{-7}$	$8.6700 \cdot 10^{-3}$	$1.2434 \cdot 10^{-9}$	$6.6274 \cdot 10^{-3}$
7	$-1.0255 \cdot 10^{-6}$	$8.5661 \cdot 10^{-2}$	$7.8557 \cdot 10^{-13}$	$3.1783 \cdot 10^{-2}$
8	$1.8394 \cdot 10^{-5}$	$2.6905 \cdot 10^{-3}$	$1.5302 \cdot 10^{-8}$	$9.6976 \cdot 10^{-4}$
9	$6.6048 \cdot 10^{-6}$	$4.3345 \cdot 10^{-3}$	$6.5721 \cdot 10^{-9}$	$1.5785 \cdot 10^{-3}$
10	$9.3724 \cdot 10^{-7}$	$1.2350 \cdot 10^{-3}$	$1.0088 \cdot 10^{-9}$	$2.3129 \cdot 10^{-4}$

IX. DISCUSSION

The attitude quaternion trajectory in Fig. 6 shows that the satellite manages to reach the reference attitude for each optimization task and with the desired angular velocity required to begin the slew maneuver or downlink, depending on the set reference. An essential property of the eclipse function $\delta(\cdot,\cdot)$ is that it gives the optimal control problem a formulation that defines where the spacecraft can and cannot harvest solar power. More specifically, with the eclipse definition, the optimal control problem defines an area, the umbra region, where the spacecraft should only consider the actuation cost. Note again that the actuation power in Fig. 11 is never negative due to the reaction wheels' inability to return electrical energy to the spacecraft. This is a significant change from [15] due to the refined formulation of the actuation power in (8).

The main results in Table VII show the amount of energy gained from the optimal control solver and the PD controller for a combination of the smaller control scenarios. There is no difference in energy with and without the imaging and communication tasks since these tasks are set identically for the optimal and the PD controller's solutions. Removing them decreases the energy gained as a percentage, from 11.3% to 6.51%. Interestingly, the longest optimization, denoted as task 7, only gives a net energy increase of 1.12%. By excluding the longest optimization from the calculations, the increase in energy becomes 39.7%. The reason for this is that the primary benefit of the proposed method comes in the transient phases, in particular, the opportunity to let the optimal solver choose when to let go of the optimal solar attitude. The energy difference values, excluding the shortest optimization, range
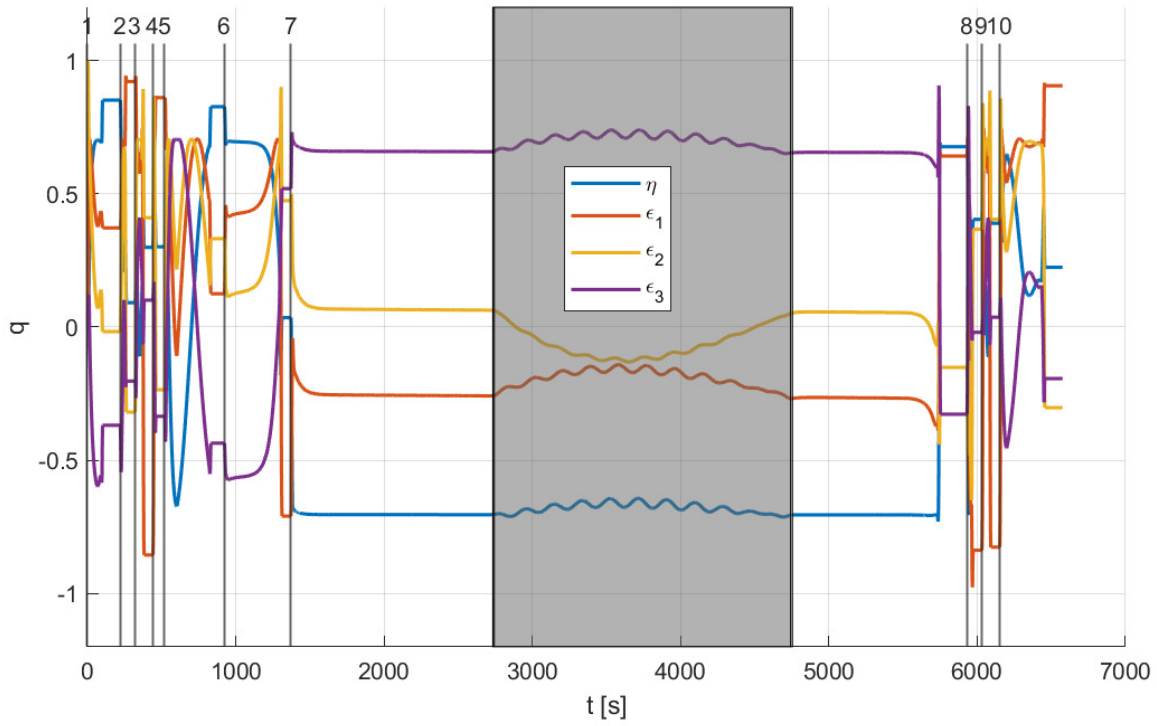
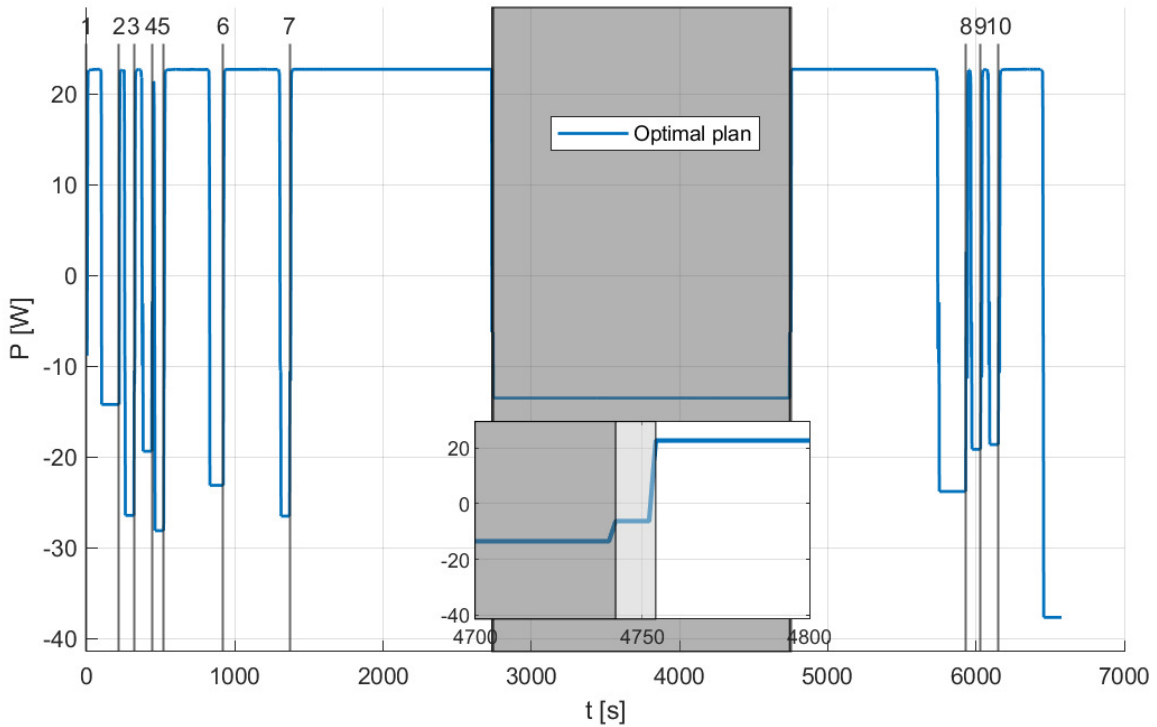Fig. 6. The optimal attitude quaternion trajectory, $\mathbf{q}_b^i$.

Fig. 7. Net power, including the loads from the other subsystems, over time. In the lower part of the figure, a zoomed-in area highlights the net power as the satellite exits the umbra and penumbra regions.
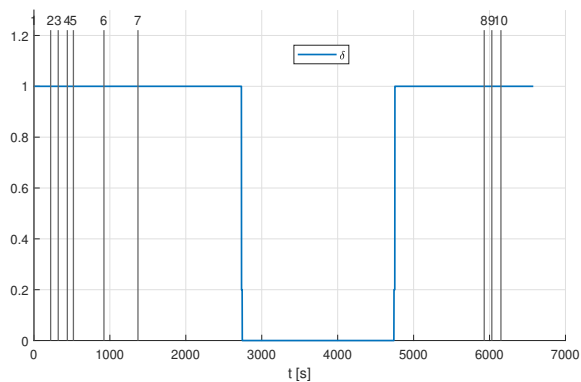
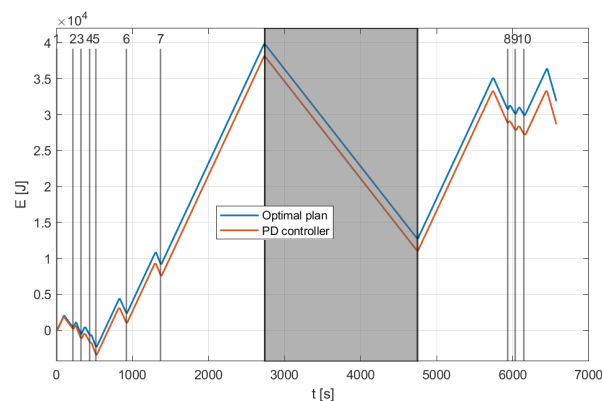Fig. 8. Solar magnitude, $\delta(\cdot,\cdot)$, over time.

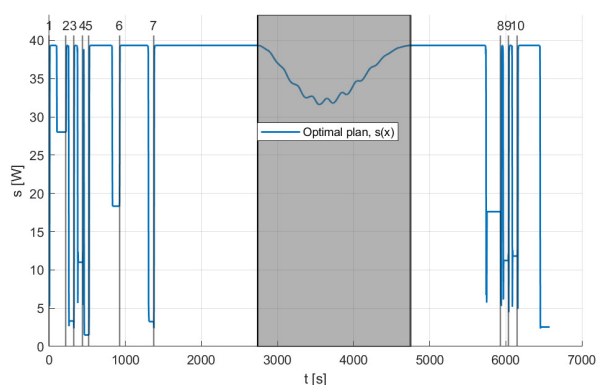Fig. 11. Cumulative values for the power terms in the cost function.

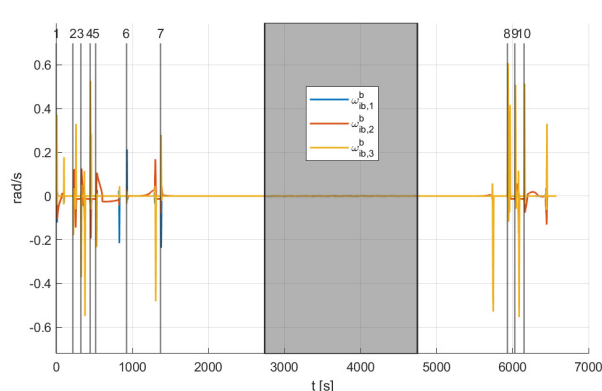Fig. 9. Solar power factor $\kappa(\cdot,\cdot)$ of the cost function over time.

Fig. 12. Angular velocity, satellite.

from about 230 J to about 600 J, no matter how long the optimization becomes. This indicates that the proposed method would be more beneficial the more frequently the imaging and communication tasks happen, or in other words, as the utilization of the satellite is increased.

Note that the one maneuver where the PD controller yields negative energy, task 4, is the shortest task. Given that the task is just 20 seconds, the PD controller does not move to a solar optimal attitude before going towards the reference.

The current scenario shows that the utilization of the satel-

lite could be higher than what is shown in this scenario: The plot in Fig. 11, which shows the cumulative energy of the satellite, only dips below zero once during the scenario, when the maneuvers are short at the beginning of the scenario. For the rest of the scenario, there is a surplus of energy. Because of this, it can be concluded that the satellite can be utilized more for imaging and downlink than what is presented in this scenario.

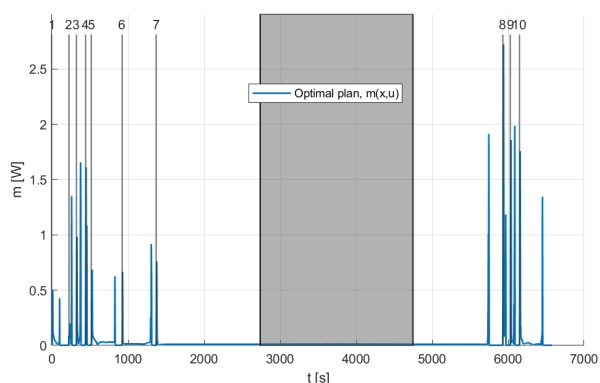As can be seen by comparing the net power plot in Fig. 7

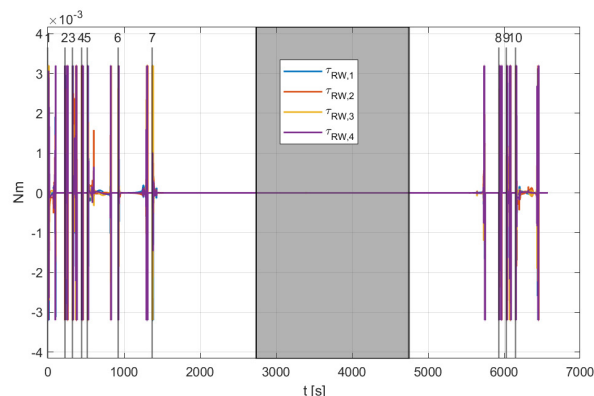Fig. 10. Actuation power part of the cost function over time.

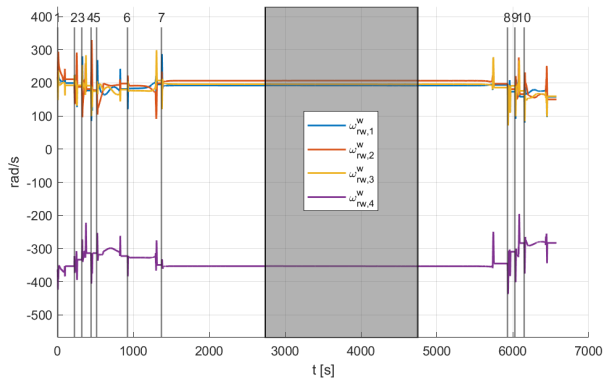Fig. 13. Torques from reaction wheels.
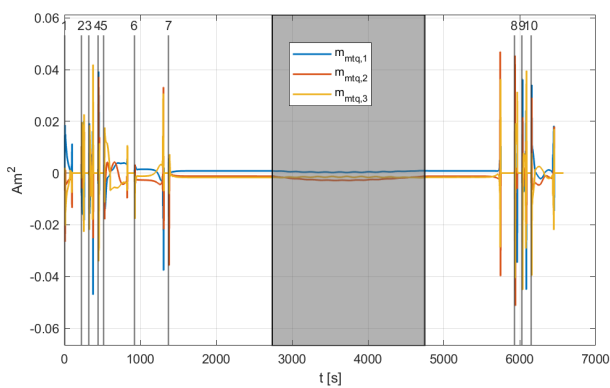
Fig. 14.   Angular velocity, reaction wheels.

Fig. 15.   Torque from magnetorquers.

to the pure solar power plot in Fig. 9, the introduction of the $\delta(\cdot,\cdot)$ function that properly describes the eclipse represents a drop in the net power when the satellite is in the shadow. This drop is equivalent to the area between the blue line in Fig. 7 when in the penumbra and the umbra region, the two different types of gray-shaded regions, and the plot's maximum value before the eclipse, which was about 22.7 W. If the sunlight could make it through the solid Earth, as using value one for the function as it would have been in [15], the total energy
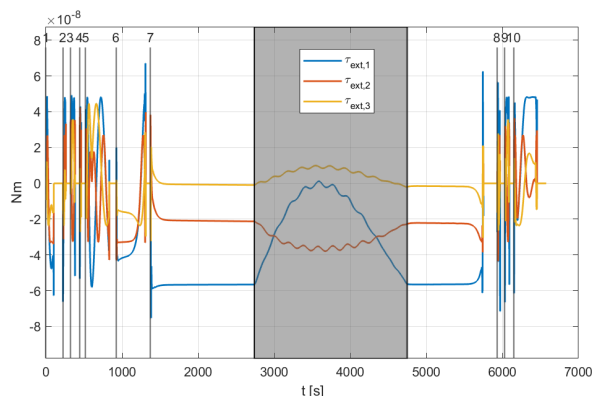

Fig. 16.   Perturbing torques.

gained would erroneously have been around 73 kJ higher for task 7. This, of course, comes from the fact that the rotations that appear in the umbra region, which, among other things, can be seen in the solar power plot in Fig. 9, would not appear for task 7 if the delta function was one.

The rotations that appear in the umbra region have two causes: they are both due to the existence of external torques and due to the nature of the numerical optimization. With the way the cost function is constructed, owing to the gyroscopic term in the system's dynamics, i.e., (12c), finding a solution where the control torque is held at precisely zero, is difficult for the solver, even without other torques affecting the satellite. Efforts can be made to mitigate this effect, such as choosing a set of body frame axes that align with the principal axes of inertia, but the external torques will remain.

A possible limitation of the approach presented in this paper is the time spent computing the optimal trajectory, as can be seen in Table VI. A spacecraft like HYPSO-2, with the parameters for the orbit presented in Table IV, orbits the Earth about once every 90 minutes and would go into these energy harvesting phases twice during an orbit. In the time it now takes to calculate one single trajectory, the satellite would require several passes if the time needed to construct the problem in CasADi before solving it is included. For this reason, efforts should be made to reduce the time required for calculating the optimal attitude trajectories. A possible avenue towards this goal includes precomputing the position and velocity of the satellite. This is expected to work well, except in a few exceptional cases: Suppose so high accuracy is required that the perturbations in orbital positions dependent on satellite attitude, which were not included in this paper, must be considered. Precomputing the position and velocity will not be an option in that case. Similarly, precomputing the position and velocity of the satellite would not work if the satellite is equipped with thrusters and performs a maneuver during the optimization.

The torque the magnetorquers produces is calculated by the control algorithm in (15). The optimal solver could also calculate this torque. It is possible to include the magnetorquer torque formulation into the optimal control problem and let the solver figure out how much torque the magnetroquers should produce. In this paper, the formulation given in (15) is preferred to limit the computation time for the optimal control trajectory.

X. Conclusion

The net power function introduced in [15] has been extended to include the environmental effects the spacecraft experiences in space, a second actuator, and the $\delta(\cdot,\cdot)$ function that describes the magnitude of the solar irradiance as a function of where the spacecraft is in its orbit. In particular, the net energy optimization performs as desired when the control horizon approaches a complete orbit when the spacecraft traverses both the umbra and penumbra regions of the orbit. The results show that the optimized solution is increasingly beneficial when the time between each maneuver decreases.

APPENDIX

Three types of perturbations are included in the simulations in this paper to make the simulated environment more realistic: Gravity gradient, magnetic torque, and eddy current torque.

The gravity gradient torque comes from the change in the pull due to different parts of the spacecraft body being in different places in the gravity field and is defined as [30]

$$\boldsymbol{\tau}_{\text{grav}}^b = 3\frac{\mu}{\|\mathbf{r}^i\|^3}\mathbf{S}\left(\frac{\mathbf{r^i}}{\|\mathbf{r}^i\|}\right)\mathbf{J}\frac{\mathbf{r^i}}{\|\mathbf{r}^i\|}. \tag{22}$$

The magnetic torque is due to the spacecraft carrying electronic equipment that sets up a magnetic field that interacts with Earth's magnetic dipole. The torque is defined as

$$\boldsymbol{\tau}_{\text{mag}}^b = \mathbf{S}(\mathbf{m}_{\text{res}}^b)\mathbf{B}^b, \tag{23}$$

where $\mathbf{B}^b$ is the magnetic field of the Earth represented in body frame coordinates, and $\mathbf{m}_{\text{res}}^b$ is the residual magnetic dipole vector. Note that while the physical principle used here is the same as is used to control the spacecraft with magnetorquers, the residual magnetic dipole $\mathbf{m}_{res}^b$ is separate from the dipole set up from the magnetorquers.

The eddy current torque is given as [30]

$$\boldsymbol{\tau}_{\text{eddy}}^b = -k_{\text{eddy}}\mathbf{S}(\mathbf{B}^b)\mathbf{S}(\boldsymbol{\omega}_{ib}^b)\mathbf{B}^b, \tag{24}$$

where k_{eddy} is a positive constant.

We assume the torque from atmospheric drag and solar radiation pressure can be omitted, which is typical e.g., for a CubeSat where the center of mass needs to be in the geometric center of the satellite.

The total environmental torque $\boldsymbol{\tau}_{\text{ext}}^b$ is the sum of the torques introduced in (22) and (23). In equation form, this gives

$$\boldsymbol{\tau}_{\text{ext}}^b = \boldsymbol{\tau}_{\text{grav}}^b + \boldsymbol{\tau}_{\text{mag}}^b + \boldsymbol{\tau}_{\text{eddy}}^b. \tag{25a}$$

REFERENCES

[1] J.-Y. Wen and K. Kreutz-Delgado, "The attitude control problem," *IEEE Transactions on Automatic Control*, vol. 36, no. 10, pp. 1148–1162, Oct. 1991.

[2] T. Lee, M. Leok, and N. H. McClamroch, "Time optimal attitude control for a rigid body," in *Proceedings of the 2008 American Control Conference*, Jun. 2008, pp. 5210–5215.

[3] H. Shen and P. Tsiotras, "Time-Optimal Control of Axisymmetric Rigid Spacecraft Using Two Controls," *Journal of Guidance, Control, and Dynamics*, vol. 22, no. 5, pp. 682–694, 1999.

[4] A. Olivares and E. Staffetti, "Time-Optimal Attitude Scheduling of a Spacecraft Equipped with Reaction Wheels," *International Journal of Aerospace Engineering*, vol. 2018, Apr. 2018.

[5] E. Sin, M. Arcak, S. Nag, V. Ravindra, A. Li, and R. Levinson, "Attitude Trajectory Optimization for Agile Satellites in Autonomous Remote Sensing Constellation," in *AIAA Scitech 2021 Forum*. AIAA, Jan. 2021.

[6] M. Krstic and P. Tsiotras, "Inverse optimal stabilization of a rigid spacecraft," *IEEE Transactions on Automatic Control*, vol. 44, no. 5, pp. 1042–1049, May 1999.

[7] W. Luo, Y.-C. Chu, and K.-V. Ling, "Inverse optimal adaptive control for attitude tracking of spacecraft," *IEEE Transactions on Automatic Control*, vol. 50, no. 11, pp. 1639–1654, Nov. 2005.

[8] J. D. Biggs and L. Colley, "Geometric Attitude Motion Planning for Spacecraft with Pointing and Actuator Constraints," *Journal of Guidance, Control, and Dynamics*, vol. 39, no. 7, pp. 1672–1677, 2016.

[9] H. C. Marsh, M. Karpenko, and Q. Gong, "Relationships Between Maneuver Time and Energy for Reaction Wheel Attitude Control," *Journal of Guidance, Control, and Dynamics*, vol. 41, no. 2, pp. 335–348, 2018.

[10] D. P. Lubey and H. Schaub, "Instantaneous Quadratic Power-Optimal Attitude Tracking with N Control Moment Gyroscopes," *Journal of Guidance, Control, and Dynamics*, vol. 40, no. 3, pp. 702–709, 2017.

[11] C. Pukdeboon and A. S. I. Zinober, "Control Lyapunov function optimal sliding mode controllers for attitude tracking of spacecraft," *Journal of the Franklin Institute*, vol. 349, no. 2, pp. 456–475, Mar. 2012.

[12] H. Schaub and V. J. Lappas, "Redundant Reaction Wheel Torque Distribution Yielding Instantaneous L2 Power-Optimal Spacecraft Attitude Control," *Journal of Guidance, Control, and Dynamics*, vol. 32, no. 4, pp. 1269–1276, 2009.

[13] C. Wu and X. Han, "Energy-optimal spacecraft attitude maneuver path-planning under complex constraints," *Acta Astronautica*, vol. 157, pp. 415–424, Apr. 2019.

[14] C. A. Rigo, L. O. Seman, E. Camponogara, E. Morsch Filho, and E. A. Bezerra, "Task scheduling for optimal power management and quality-of-service assurance in CubeSats," *Acta Astronautica*, vol. 179, pp. 550–560, Feb. 2021.

[15] B. A. Kristiansen, J. T. Gravdahl, and T. A. Johansen, "Energy optimal attitude control for a solar-powered spacecraft," *European Journal of Control*, 2021.

[16] D. A. Vallado, *Fundamentals of astrodynamics and applications*. Springer Science & Business Media, 2001, vol. 12.

[17] M. E. Grøtte, R. Birkeland, E. Honoré-Livermore, S. Bakken, J. L. Garrett, E. F. Prentice, F. Sigernes, M. Orlandić, J. T. Gravdahl, and T. A. Johansen, "Ocean color hyperspectral remote sensing with high resolution and low latency—the HYPSO-1 CubeSat mission," *IEEE Transactions on Geoscience and Remote Sensing*, vol. 60, pp. 1–19, 2022.

[18] B. A. Kristiansen, M. E. Grøtte, and J. T. Gravdahl, "Quaternion-based generalized super-twisting algorithm for spacecraft attitude control," in *Proceedings of the 21st IFAC World Congress*, 2020.

[19] M. E. Grøtte, J. T. Gravdahl, T. A. Johansen, J. A. Larsen, E. M. Vidal, and E. Surma, "Spacecraft attitude and angular rate tracking using reaction wheels and magnetorquers," *IFAC-PapersOnLine*, vol. 53, no. 2, pp. 14 819–14 826, 2020.

[20] J. A. E. Andersson, J. Gillis, G. Horn, J. B. Rawlings, and M. Diehl, "CasADi – A software framework for nonlinear optimization and optimal control," *Mathematical Programming Computation*, vol. 11, no. 1, pp. 1–36, 2019.

[21] 6u nanosatellite bus m6p. [Online]. Available: https://nanoavionics.com/small-satellite-buses/6u-nanosatellite-bus-m6p/

[22] B. Neta and D. Vallado, "On satellite umbra/penumbra entry and exit positions," vol. 46, no. 1, pp. 91–103.

[23] D. Huynh, "Metrics for 3d rotations: Comparison and analysis," *Journal of Mathematical Imaging and Vision*, vol. 35, pp. 155–164, 10 2009.

[24] O. Egeland and J. T. Gravdahl, *Modeling and simulation for automatic control*. Marine Cybernetics Trondheim, Norway, 2002.

[25] S. Gros, M. Zanon, and M. Diehl, "Baumgarte stabilisation over the SO(3) rotation group for control," in *Proceedings of the 54th IEEE Conference on Decision and Control*. IEEE, Dec. 2015, pp. 620–625.

[26] F. L. Markley and J. L. Crassidis, *Fundamentals of spacecraft attitude determination and control*. Springer, 2014.

[27] A. Wächter and L. T. Biegler, "On the implementation of an interior-point filter line-search algorithm for large-scale nonlinear programming," *Mathematical Programming*, vol. 106, no. 1, pp. 25–57, Mar. 2006.

[28] P. Alken, E. Thébault, C. D. Beggan, H. Amit, J. Aubert, J. Baerenzung, T. N. Bondar, W. J. Brown, S. Califf, A. Chambodut, A. Chulliat, G. A. Cox, C. C. Finlay, A. Fournier, N. Gillet, A. Grayver, M. D. Hammer, M. Holschneider, L. Huder, G. Hulot, T. Jager, C. Kloss, M. Korte, W. Kuang, A. Kuvshinov, B. Langlais, J.-M. Léger, V. Lesur, P. W. Livermore, F. J. Lowes, S. Macmillan, W. Magnes, M. Mandea, S. Marsal, J. Matzka, M. C. Metman, T. Minami, A. Morschhauser, J. E. Mound, M. Nair, S. Nakano, N. Olsen, F. J. Pavón-Carrasco, V. G. Petrov, G. Ropp, M. Rother, T. J. Sabaka, S. Sanchez, D. Saturnino, N. R. Schnepf, X. Shen, C. Stolle, A. Tangborn, L. Tøffner-Clausen, H. Toh, J. M. Torta, J. Varner, F. Vervelidou, P. Vigneron, I. Wardinski, J. Wicht, A. Woods, Y. Yang, Z. Zeren, and B. Zhou, "International geomagnetic reference field: the thirteenth generation," *Earth, Planets and Space*, vol. 73, no. 1, p. 49, 2021.

[29] J. Davis, "Mathematical Modeling of Earth's Magnetic Field," 2004.

[30] P. C. Hughes, *Spacecraft Attitude Dynamics*. Dover Publications, Inc., 2004.

Bjørn Andreas Kristiansen (Member, IEEE) received his M.Sc. and Ph.D. degrees from the Norwegian University of Science and Technology in 2019 and 2023, respectively. He is currently a postdoctoral researcher at the NTNU SmallSat lab and the Department of Engineering Cybernetics in Trondheim, Norway. His current research concerns optimal attitude control, with a specific focus on optimal control for attitude maneuvers with respect to energy and time in the context of agile satellite operations.

Tor Arne Johansen (Senior Member, IEEE) received the M.Sc. and Ph.D. degrees in electrical and computer engineering from the Norwegian University of Science and Technology (NTNU), Trondheim, Norway, in 1989 and 1994, respectively.

From 1995 to 1997, he worked at SINTEF as a Researcher before he was appointed Associated Professor with the NTNU, in 1997, and a Professor in 2001. He has published several hundred articles in the areas of control, estimation and optimization with applications in the marine, aerospace, automotive, biomedical and process industries. In 2002, he cofounded the company Marine Cybernetics AS, Trondheim, where he was a Vice President until 2008.

Dr. Johansen received the 2006 Arch T. Colwell Merit Award of the SAE and is a Principal Researcher within the Center of Excellence on Autonomous Marine Operations and Systems (NTNU-AMOS), Trondheim, and the Director of the Unmanned Aerial Vehicle Laboratory at NTNU and the SmallSat Laboratory at NTNU. He recently cofounded the spin-off companies Scout Drone Inspection, UBIQ Aerospace, Zeabuz and SentiSystems.
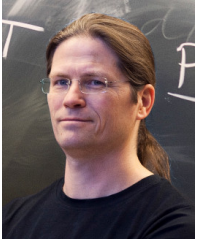
Jan Tommy Gravdahl (Senior Member, IEEE) received the Siv.Ing. and Dr.Ing. degrees in engineering cybernetics from the Norwegian University of Science and Technology (NTNU), Trondheim, Norway, in 1994 and 1998, respectively.

He was appointed Associate Professor and Professor with the Department of Engineering Cybernetics, NTNU, in 2001 and 2005, respectively. He was the Head of the Department of Engineering Cybernetics from 2008 to 2009. He has supervised the graduation of 160 M.Sc. and 20 Ph.D. candidates. He has published five books and more than 300 articles in international conferences and journals. His research interests include mathematical modeling and nonlinear control in general, in particular applied to turbomachinery, marine vehicles, spacecraft, robots, and high-precision mechatronic systems.

Dr. Gravdahl received the IEEE Transactions on Control Systems Technology Outstanding Paper Award in 2000 and 2017. He was Senior Editor of the IFAC journal Mechatronics in the period 2017-22 and is since 2020 Associate Editor of the IEEE Transactions on Control Systems Technology.

Sébastien Gros received the Ph.D. degree from EPFL, Lausanne, Switzerland, in 2007. After a journey by bicycle from Switzerland to the Everest base camp in full autonomy, he joined a Research and Development Group hosted at Strathclyde University, Glasgow, U.K., focusing on wind turbine control. In 2011, he joined the University of KU Leuven, Leuven, Belgium, where his main research focus was on optimal control and fast MPC for complex mechanical systems. He joined the Department of Signals and Systems, Chalmers University of Technology, Gothenburg, Sweden, in 2013, where he became an Associate Professor, in 2017. He is currently a Full Professor with NTNU, Trondheim, Norway, and a Guest Professor with Chalmers, Gothenburg. His main research interests include numerical methods, real-time optimal control, reinforcement learning, and the optimal control of energy-related applications.